chemosensors

MDPI

Article

Electrodes for Paracetamol Sensing Modified with Bismuth Oxide and Oxynitrate Heterostructures: An Experimental and Computational Study

Filippo Franceschini [1,2], Mattia Bartoli [3,4,*], Alberto Tagliaferro [1,4] and Sandro Carrara [2,*]

1 Department of Applied Science and Technology, Politecnico di Torino, 10129 Turin, Italy; flp.franceschini@studenti.polito.it (F.F.); alberto.tagliaferro@polito.it (A.T.)
2 Bio/CMOS Interfaces Group, Integrated Circuits Laboratory (ICLAB), EPFL, CH-2002 Neuchatel, Switzerland
3 Center for Sustainable Future Technologies, Italian Institute of Technology, Via Livorno 60, 10144 Turin, Italy
4 Consorzio Interuniversitario Nazionale per la Scienza e Tecnologia dei Materiali (INSTM), 50121 Florence, Italy
* Correspondence: mattia.bartoli@polito.it (M.B.); sandro.carrara@epfl.ch (S.C.); Tel.: +39-0110907346 (M.B.); +41-216930915 (S.C.)

Abstract: In this work, novel platforms for paracetamol sensing were developed by the deposition of Bi_2O_3, $Bi_5O_7NO_3$ and their heterostructures onto screen-printed carbon-paste electrodes. An easy and scalable solid state synthesis route was employed, and by setting the calcination temperatures at 500 °C and 525 °C we induced the formation of heterostructures of Bi_2O_3 and $Bi_5O_7NO_3$. Cyclic voltammetry measurements highlighted that the heterostructure produced at 500 °C provided a significant enhancement in performance compared to the monophases of Bi_2O and $Bi_5O_7NO_3$, respectively. That heterostructure showed a mean peak-to-peak separation E_p of 411 mV and a sensitivity increment of up to 70% compared to bare electrodes. A computational study was also performed in order to evaluate the geometrical and kinetic parameters of representative clusters of bismuth oxide and subnitrate when they interact with paracetamol.

Keywords: bismuth; paracetamol; electrochemical sensor; electron transfer rate; screen-printed electrode

Citation: Franceschini, F.; Bartoli, M.; Tagliaferro, A.; Carrara, S. Electrodes for Paracetamol Sensing Modified with Bismuth Oxide and Oxynitrate Heterostructures: An Experimental and Computational Study. *Chemosensors* **2021**, *9*, 361. https://doi.org/10.3390/chemosensors9120361

Academic Editors: Ali Othman and Gyözö G. Láng

Received: 10 November 2021
Accepted: 15 December 2021
Published: 17 December 2021

1. Introduction

Paracetamol (PCM) is one of the most commonly consumed drugs in the world, being used as an antipyretic, analgesic, and non-steroidal anti-inflammatory compound [1]. The mechanism of its action is still under study [2], while evidence shows the inhibition of the cyclooxygenase activity in the brain and the synthesis of prostaglandins [3]. Under the correct therapeutic dosage, no side effects are reported. However, liver and kidney damage are a frequent consequence in the case of overdose [4]. As reported in Stravitz et al. [5], PCM toxicity is the main cause of acute liver failure in the U.S., which leads to a liver transplant for approximately 30% of the cases. Furthermore, PCM is considered an emerging freshwater pollutant by Murray et al. [6], based on a number of criteria such as its toxicity to aquatic organisms and its environmental persistence. This problem is exacerbated by the fact that many waste treatment facilities are not capable of adequately detecting and removing its toxic degradation products [7]. Some of the treatment methods to remove PCM use photo–electro–Fenton oxidation, activated charcoal, ultrafiltration and ozone oxidation [8]. It has been reported that the presence of PCM or its degradation products in water can induce neurotoxic effects on aquatic organisms [9], by inhibiting acetylcholinesterase. Additionally, even if the concentration of this particular xenobiotic is relatively low, Elersek et al. [10] showed that the presence of other drugs with a similar mode of action can lead to synergistic interactions, increasing the risk of toxic effects.

Consequently, given its role as a freshwater pollutant and its toxic effects on the liver with overdoses, the development of effective detection techniques is of paramount importance.

Among the wide range of analytical tools, electrochemical sensors have shown significant advantages over other techniques (i.e., HPLC, spectrophotometry, colorimetry and chemiluminescence) due to their ability to provide cheap, fast, easy-to-use and in-line measurements [11]. An effective approach to improving the sensitivity and electrooxidation kinetics of electrochemical sensors is to employ nanostructured catalysts [12,13]. Furthermore, multiple studies have now shown a clear size-dependence of the catalytic activity that may briefly be ascribed to surface-enhancement and quantum effects [14,15], with detectable amounts ranging from 1–2 nM [16,17] up to 3 μM [18]. Noble metal nanoparticles, especially Au, Pd and Pt, show exceptional electrocatalytic behavior, decreased overpotentials in relevant electrochemical reactions and even an improved reversibility [19]. Unfortunately, the use of noble metals is usually prohibitive for many applications due to the materials' cost. For this reason, an interesting alternative is offered by metal oxides, which have shown promising results in the oxidation of aromatic compounds [20]. In particular, the introduction of structural defects (i.e., substitutional atoms or oxygen vacancies in metal oxides) can alter the electronic structure and improve the electrochemical performance [21]. Consequently, a metal oxide with accurately designed defects could show significant improvements in its electrochemical activity. Among all the available metal oxide species, bismuth-based materials show a wide range of oxide phases easily produced through thermal routes [22], displaying a notable performance as photocatalysts [23]. In this work, bismuth oxide and a bismuth subnitrate are evaluated as potential electroactive materials for PCM detection. Our focus is the synergistic effects of their heterostructures as produced through solid-state synthesis routes: Bi_2O_3, $Bi_5O_7NO_3$ and their heterostructures were deposited onto screen-printed electrodes (SPE) and tested through cyclic voltammetry. The modified SPEs were characterized both in terms of their kinetics and sensitivity. Furthermore, a computational study based on semiempirical methods was performed to evaluate the geometrical and energetic parameters of the transitional state.

2. Materials and Methods

2.1. Materials

Bismuth nitrate pentahydrate $Bi(NO_3)_3{\cdot}5H_2O$ was purchased from Sigma Aldrich (Burlington, MA, USA). Paracetamol was purchased in powder form with a purity higher than 98% (Sigma Aldrich). Phosphate Buffered Saline (PBS) tablets were purchased as well (Sigma Aldrich). The deionized water was subject to a bi-distillation process.

2.2. Bismuth Subnitrate Heterostructures Synthesis

Following the procedure reported by Kodama [24] and Gadhi et al. [23], heterostructures of Bi_2O_3 and $Bi_5O_7NO_3$ were produced via a simple solid state method using as a precursor salt $Bi(NO_3)_3{\cdot}5H_2O$. First, the precursor salt was ground in a mortar. The pulverized precursor was heated in a tubular furnace (Carbolite TZF 12/65/550) at 200 °C in a nitrogen atmosphere for one hour to obtain a complete dehydration. Afterwards, the temperature was raised to 300 °C and maintained for two hours. In the last step of the process, the temperature was kept between 400 and 600 °C, depending on the degree of oxidation targeted. Four different kinds of samples were synthesized at distinct calcination temperatures, as shown in Table 1. Afterward, all of the samples were cooled in air, to promote the formation of β-Bi_2O_3. For all the described steps, the heating ramp was set to 10 °C/min. The samples were labelled as Bxxx, where xxx represents the final step temperature in °C.

The samples were analyzed with a Renishaw Invia confocal Raman spectrometer with an exciting CW laser of 514 nm at a temperature of 298 K in the range 500–3500 cm^{-1}.

Sample morphology was investigated using high-resolution field emission scanning electron microscopy (FE-SEM) (Supra 40 microscope, Zeiss, Oberkochen, Germany).

Table 1. Thermal treatment used for the synthesis of bismuth oxide and bismuth subnitrate structures.

	Dehydration (1 h)	2° Step (2 h)	3° Step (1 h)
B450	200 °C	300 °C	450 °C
B500	200 °C	300 °C	500 °C
B525	200 °C	300 °C	525 °C
B600	200 °C	300 °C	600 °C

2.3. Working Electrode Modification

The synthesized materials were used to decorate a commercial SPE (Dropsens DRP110C), following the procedure reported by Madagalam et al. [25]. Well-dispersed suspensions of synthesized materials were prepared by adding around 12 mg of material to 4 mL of distilled water and ultrasonically treated for 10 min. SPEs with a carbon-based working electrode (with area of up to around 0.12 cm^2), a carbon-based counter electrode, and silver pseudo-reference electrode were used as electrochemical sensors. The potential of the pseudo-reference electrode was stable under the conditions and timescale used in the experiments. SPEs were modified by the drop-casting technique, spreading 5 µL of bismuth species suspension on the surface of the working electrode, and drying overnight at room temperature. Bare and modified SPEs were stored under atmospheric conditions after the surface modification.

2.4. Electrochemical Measurements

A cyclic voltammetry study was performed using an Autolab potentiostat under atmospheric conditions. A volume of 100 µL of PCM solution (0.1 M of PBS + 1 mM PCM) at pH 7.4 was dropped onto the surface of the working electrode by means of a micropipette. The potential was swept from −0.3 V to 0.9 V and the scan rate was varied between 0.1 V/s and 0.3 V/s in steps of 0.05 V/s. Calibration curves were produced by acquiring multiple voltammograms at 0.1 V/s using concentrations of PCM (0.5 mM, 1 mM, 2 mM, 3 mM) in 0.1 M of PBS. All measurements were replicated three times and the results reported as average values with related uncertainty.

For each voltammogram, the baseline was removed with Matlab, following known approaches [26], to ensure that only faradaic currents were considered.

2.5. Computational Study

Clusters of Bi_2O_3 and $Bi_5O_7NO_3$ were defined according to their unit cells and then modified appropriately to compensate for the lack of border atoms (and thus they were in a state of undervalence), according with Harwing [27] and Ziegler et al. [28], respectively. For Bi_2O_3, the crystal structure of reference was the tetragonal one, which was most likely that of the synthesized bismuth oxide. The clusters were first roughly defined with the use of the software Avogadro and subsequently optimized with the commercial software Hyperchem 8.0.1. The optimization was performed with the semiempirical Parametric Method 3 (PM3) using an optimization algorithm based on the conjugate gradient (Polak–Ribiere) with a set limit of energy convergence of 0.01 kcal/(Åmol) [29]. For each cluster, the interaction with a molecule of PCM was evaluated. Five water molecules were added in both cases to account at least partially for solvation effects. Both systems were thus optimized with PM3. The resulting configurations were considered hypothetical transition states for the electron transfer between PCM and the respective cluster. In this way, it was possible to apply the generalized theory of Marcus [30,31] and to estimate the rate constant of the electron transfer.

3. Results

3.1. Characterization of Bismuth-Based Heterostructures through Raman Spectroscopy

In Figure 1, the Raman spectra of the synthesized materials are reported.

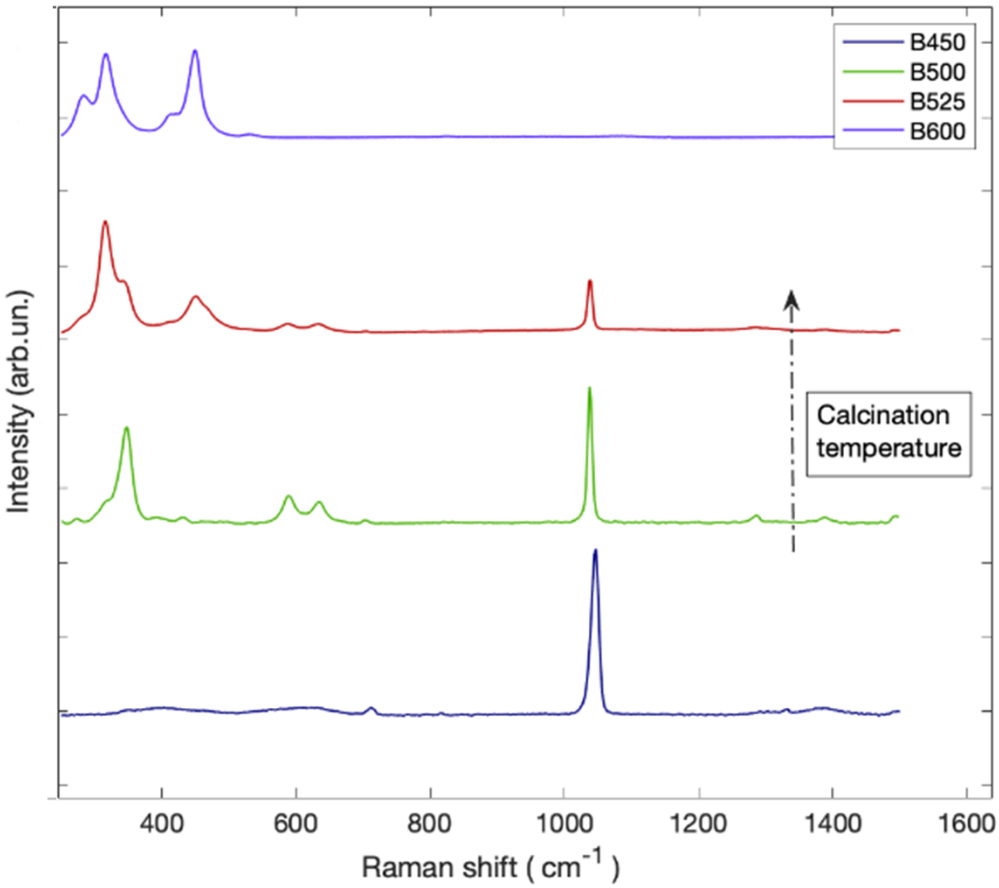

Figure 1. Raman spectra of the synthesized materials. From bottom to top: B450, B500, B525, B600.

The spectrum of sample B450 showed five bands peaking at 712 cm^{-1}, 811 cm^{-1}, 1049 cm^{-1}, 1328 cm^{-1} and 1380 cm^{-1}, respectively.

According to Xu et al. [32], the last three peaks were due to the symmetrical and asymmetrical υ_{NO} of nitro groups, while the peaks at 712 cm^{-1} (in-plane deformation), 811 cm^{-1} (out-of-plane deformation) were due to skeletal vibrations. While the peaks 1328 cm^{-1} and 1380 cm^{-1} were very low in intensity, the peak centered on 1049 cm^{-1} was very intense and could easily be used to monitor the evolution of $Bi_5O_7NO_3$ by increasing the calcination temperature. Across the temperature range investigated, the peak centered on 1049 cm^{-1} decreased according with the preliminary observation of Kodama [24] due to the thermal decomposition of nitro residues with the release of NO. The spectra of sample B600 showed bands peaking at 282 cm^{-1}, 315 cm^{-1}, 418 cm^{-1}, 448 cm^{-1} and 530 cm^{-1}, which is compatible with the reported spectrum of pure Bi_2O_3 [33,34].

The morphologies of B450 and B600 were investigated using FESEM as shown in Figure 2.

According to data reported by Gadhi et al. [23], pure $Bi_5O_7NO_3$ (Figure 2a) has a structure characterized by flower-like particles composed of interconnected planes of few nanometers in thickness. B600 showed a partial sinterization of pure Bi_2O_3 grains due to the high calcination temperatures (Figure 2b) as was reported by Balint et al. [35].

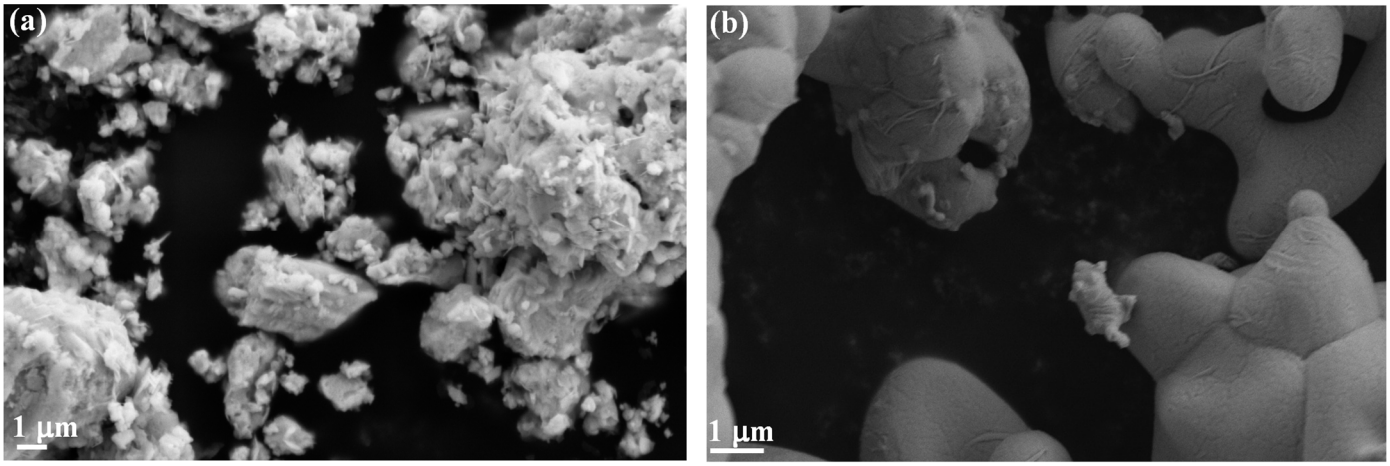

Figure 2. Scanning electron microscope captures of (**a**) B450 and (**b**) B600.

3.2. Electrochemical Measurements

Figure 3 presents the voltammograms of the modified SPEs compared to the bare electrode. The electrolytic solution was composed of 0.1 M PBS at pH 7.4 and 1 mM of PCM, and the scan rate was 0.1 V/s. In the absence of PCM, no redox peaks could be detected. Table 2 summarizes the mean anodic peak currents and the peak-to-peak distance, with their respective standard error. All of the functionalized sensors presented a higher current peak compared to the bare electrode and a reduced peak-to-peak separation (ΔE_p). The heterostructures B500 and B525 displayed even greater currents, with a reduction of ΔE_p. All the sensors showed a cathodic current peak intensity of up to around 50% of the anodic current peak. This suggests that the electrooxidation of PCM involves two electrons and two protons and is pH-dependent, as elucidated by Miner et al. [36].

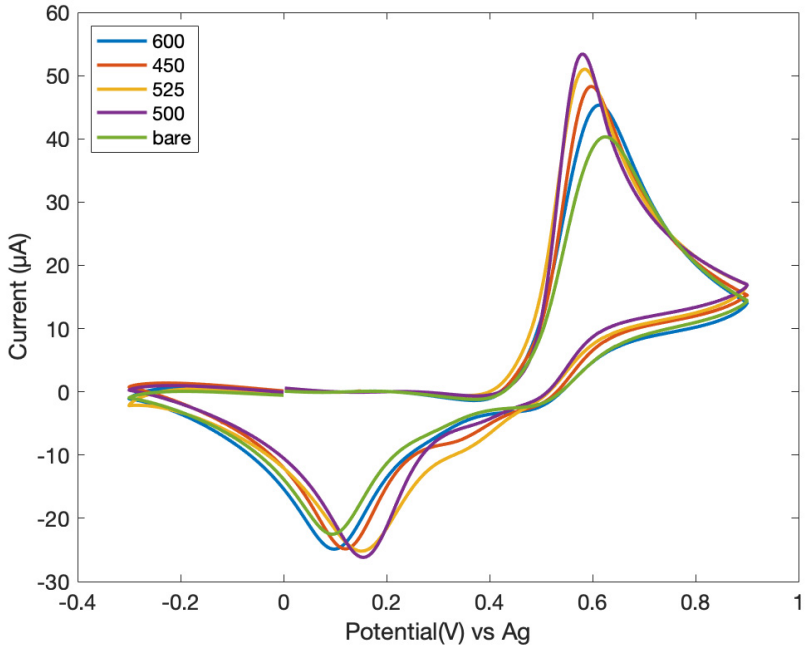

Figure 3. Voltammograms of the differently modified sensors at 0.1 V/s scan rate for an electrolytic solution of 0.1 M PBS with 1 mM PCM.

Table 2. Anodic peak and peak-to peak separations for bare electrode and modified SPEs. (0.1 V/s).

Material	Anodic Peak (μA)	ΔE_p (mV)
Bare electrode	40.2 ± 0.5	495 ± 5
B450	49.1 ± 1.2	430 ± 10
B500	52.4 ± 1.0	411 ± 10
B525	51.1 ± 0.9	418 ± 7
B600	45.3 ± 0.7	447 ± 6

Accordingly, in this study N-acetyl-p-benzoquinone-imine (NAPQI) was the main product of the oxidation of paracetamol at pH 7 and showed a tendency to form with a dimeric structure. Hence, the coupling of the dimerization chemical reaction with the electrochemical oxidation of paracetamol was most likely the cause of the lower cathodic currents.

Nematollahi et al. [37] suggested that an adsorbed layer of dimers prevents the reduction of NAPQI. Nevertheless, the linear dependence of the peak currents on the square root of the scan rate would indicate the presence of freely diffusing redox species. Moreover, an inverse dependence of I_{pc}/I_{pa} on the concentration of PCM was observed for all sensors. This indicates that a second-order reaction was taking place [26], such as a dimerization reaction.

To perform a kinetic characterization of the sensors, the voltammograms were acquired from a range of scans from 0.1 V/s to 0.3 V/s, as shown in Figure 4.

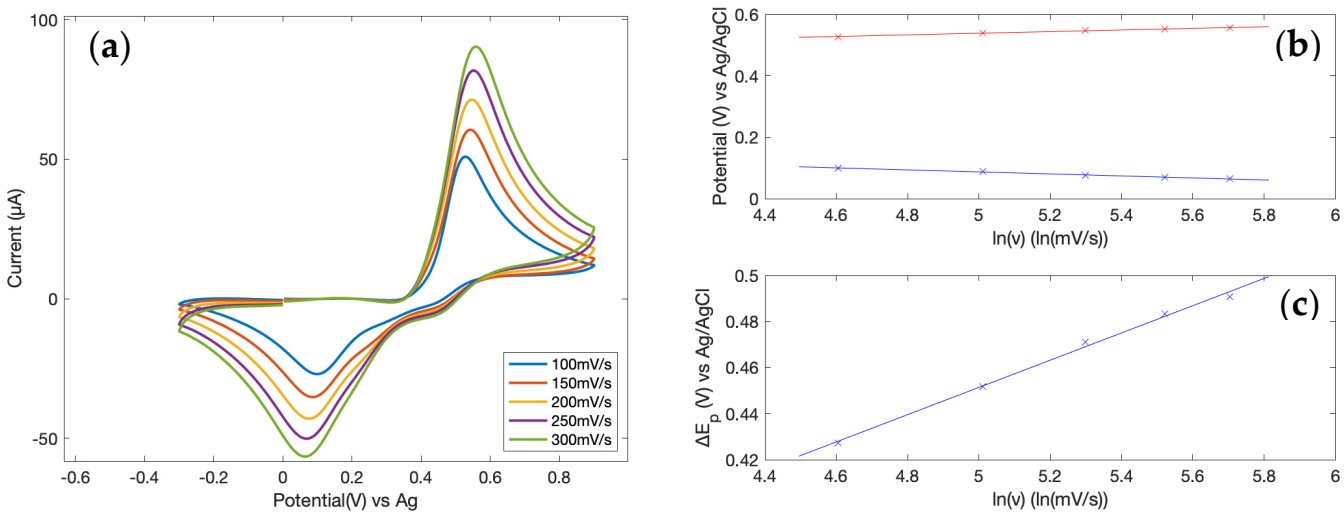

Figure 4. (**a**) Cyclic voltammograms of 1 mM PCM in 0.1 M of PBS with scan rate varied from 100 mV to 300 mV for a sensor functionalized with B500. (**b**) Linear dependence of the peak currents' positions with respect to the natural logarithm of the scan rate. (**c**) Linear dependence of the peak-to-peak separation with respect to the natural logarithm of scan rate.

A linear dependence of the peak currents (anodic and cathodic) with respect to the square root of the scan rate was observed as shown in Table 3.

Table 3. Linear regression equations ($I_{pa}vs\ \sqrt{v}$) for the different modified SPEs (scan rate = 0.1 V/s) and calculated diffusion coefficient of PCM for a scan rate of 100 mV/s.

Material	I_{pa} (μA)	R^2	D (cm^2/s)
Bare electrode	$3.84\ \sqrt{v} + 2.81$	0.996	2.92×10^{-6}
B450	$4.37\ \sqrt{v} + 5.58$	0.992	3.33×10^{-6}
B500	$5.12\ \sqrt{v} + 2.79$	0.995	3.16×10^{-6}
B525	$4.93\ \sqrt{v} + 2.85$	0.996	2.49×10^{-6}
B600	$4.29\ \sqrt{v} + 2.43$	0.995	1.96×10^{-6}

Such behavior is indicative of an electrochemical process controlled by diffusion and not by adsorption [38].

Accordingly, the Randles–Sevcik equation can thus be applied:

$$i_p = 0.446\, nFAC^0 \left(\frac{nFvD_0}{RT}\right)^{\frac{1}{2}} \quad (1)$$

where n is the number of electrons exchanged in the reaction, A is the working electrode area, C^0 is the concentration of the analyte in the bulk, D_0 is the diffusion coefficient of the redox species; the n (number of exchanged electrons) was 2, according with Nematollahi et al. [37].

The peak currents' positions E_{pa} and E_{pc} were observed to shift linearly with respect to the Napierian logarithm of the scan rate, which is indicative of a quasi-reversible process [39]. The charge transfer coefficient (α) was calculated by taking the slope of the regression line of the anodic (m_a) and cathodic (m_c) peaks' positions with respect to the logarithm of the scan rate and then by considering the following equation by Laviron [40]:

$$m_c \cdot RT \cdot \alpha nF = m_a \cdot RT \cdot (1-\alpha) nF \quad (2)$$

Similarly, with the use of the Laviron theory the rate constant of the electron transfer k was calculated with the use of the following relationship:

$$ln(k) = \alpha\, ln(1-\alpha) + (1-\alpha)\, ln\alpha - log\left(\frac{RT}{nFv}\right) - \alpha(1-\alpha)\left(\frac{nF\Delta E_p}{RT}\right) \quad (3)$$

It is worth noting that the use of the Laviron theory is compatible with the peak-to-peak distance of well over 200 mV/n observed in all samples.

Table 4 summarizes the calculated values of the electron transfer rate (k) and of the charge transfer coefficient (α). The sensors functionalized with the heterostructures (samples B500 and B525) presented superior kinetics on PCM electrooxidation with respect to the single phase samples of $Bi_5O_7NO_3$ (sample B450) Bi_2O_3 (sample B600).

Table 4. Experimental values of electron transfer and alpha for bismuth subnitrates, heterostructures and oxides as computed by the Laviron theory.

Material	k (ms^{-1})	Alpha (α)
Bare electrode	0.30 ± 0.05	0.488 ± 0.058
B450	1.11 ± 0.10	0.441 ± 0.094
B500	1.64 ± 0.08	0.418 ± 0.084
B525	1.52 ± 0.09	0.422 ± 0.065
B600	0.88 ± 0.07	0.453 ± 0.087

Gadhi et al. [18] showed that the valence and the conduction band of $\beta - Bi_2O_3$ are lower in energy compared with $Bi_5O_7NO_3$. Consequently, a Type-II heterojunction is formed as a result of the misaligned band edges at the interphase improving the charge carrier separation. These heterostructures can generate a built-in electric field that could promote the charge transfer during electrocatalytic applications [41–43]. Accordingly, the kinetics of the modified SPEs with B600 (pure Bi_2O_3) and B450 (pure $Bi_5O_7NO_3$) was found to be slower compared to those functionalized with the heterostructured materials. This was due to a combination of the electrons' mobility and particles' morphologies as shown in Figure 2a,b.

In order to fully characterize the performance of the different SPEs on PCM detection, it was important to evaluate their responses at different analyte concentrations. CV, at a scan rate of 100 mV/s, was thus performed at four different PCM concentrations (0.5 mM, 1 mM, 2 mM, 3 mM). The peak anodic current was taken for each measurement, and by

plotting those values against the molar concentration a linear regression curve could be obtained, as shown in Figure 5.

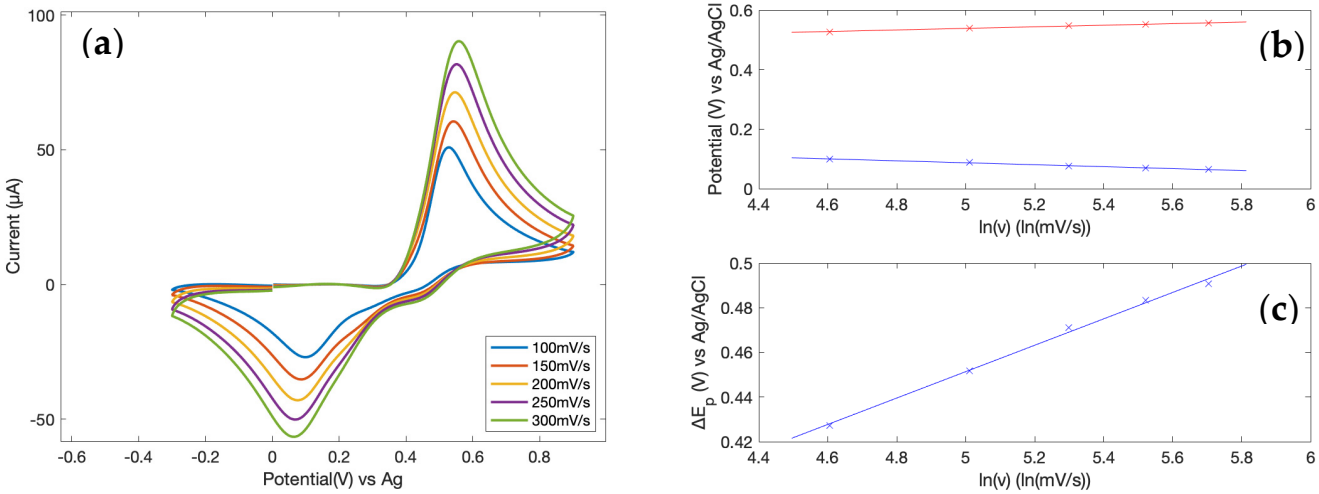

Figure 5. (**a**) Cyclic voltammograms of 1 mM PCM in 0.1 M of PBS with scan rate varied from 100 mV to 300 mV for a sensor functionalized with B525. (**b**) Linear dependence of the peak currents' positions with respect to the natural logarithm of the scan rate. (**c**) Linear dependence of the peak-to-peak separation with respect to the natural logarithm of the scan rate.

Figure 6 shows the different calibration curves of the bare and functionalized electrodes. From the slopes of the curves, sensitivity values were obtained, and the Standard Deviation (SD) for the three samples calculated. The SD was then divided by the square root of the number of samples to obtain the standard error of the mean.

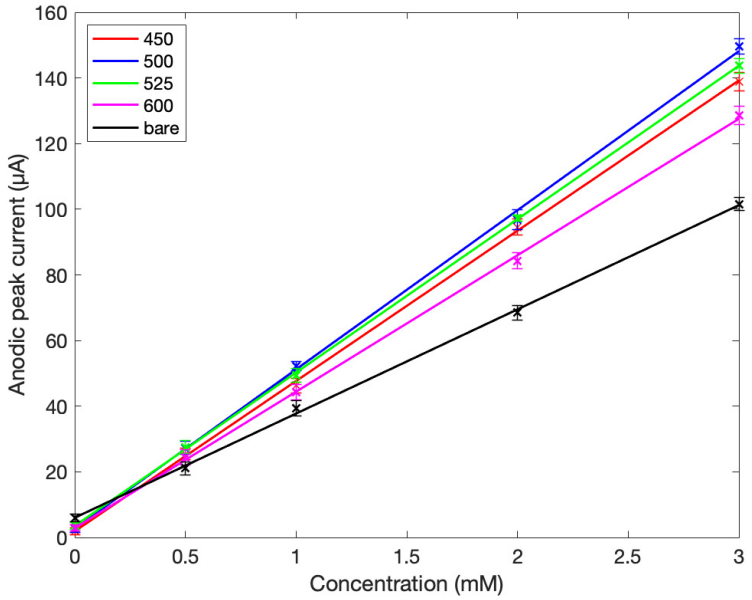

Figure 6. Calibration curves for the bare electrode, B450, B500, B525, and B600 obtained by plotting the anodic peak currents at 100 mV/s with respect to the different concentrations of PCM.

It can clearly be seen that the deposition of bismuth oxide/bismuth subnitrate species greatly improved the sensitivity of the sensors. The B500-modified sensor had a sensitivity of 48.47 ± 0.32 μA/mM, while the B525-modified one had a sensitivity of 46.73 ± 0.28 μA/mM, almost twice the reported value for the bare electrode. This is likely due to a higher surface area arising from the nanoflake morphology of the synthesized heterostructures (as

reported by Gadhi et al. [23]) and also simply the presence of more favorable sites for the adsorption related to the presence of interphases.

The limit of detection (LOD) is the minimum amount of a species that can be detected by a sensor from the blank measurement (in the absence of the analyte) within a certain confidence interval. To calculate the LOD for the different sensors in Table 5, the following formula was used:

$$LOD = \frac{K \times \sigma_x}{S} \quad (4)$$

where σ_x is the standard deviation of the blank measurement, S is the calculated sensitivity, $K = 3$ is a constant that depends on the desired confidence interval (here 99.6%).

Table 5. Sensitivity and limit of detection.

Material	Sensitivity (μA/mM)	LOD (μM)
Bare electrode	28.83 ± 0.15	3.642 ± 0.019
B450	45.78 ± 0.33	4.484 ± 0.032
B500	48.47 ± 0.32	4.209 ± 0.028
B525	46.73 ± 0.28	4.391 ± 0.036
B600	41.56 ± 0.24	4.714 ± 0.028

Surprisingly, the LOD of the functionalized sensors was slightly higher than for the bare electrode, even though the sensitivity (at the denominator) was greater. The different responses of the modified electrodes to the blank solution led to larger standard deviations, which caused a modest increase in the LOD.

Furthermore, it is interesting to note that the capacitive current also significantly changed with the structuration of the SPEs. In addition, Figure 2 shows a decreased offset current moving from the base electrodes to sample B450, while the apparent differences among the four samples were not statistically significant. Therefore, we cannot conclude that the two heterostructures improved the capacitive current more than the single phase samples, while we can conclude that all of the functionalizations with bismuth improved the capacitive current with respect to the base SPE.

3.3. Computational Study

The interaction between a modified SPE's surface and bismuth clusters is a key point for understanding such a system, and could lead to further improvements in tailoring the structure. Accordingly, we evaluated the electron transfer rate and the geometrical parameters of two representative bismuth structures, Bi_2O_3 and $Bi_5O_7NO_3$, as shown in Figure 7.

By using the generalized Marcus theory as developed by Tachiya et al. [31], we estimated the rate constant of the electron transfer k using Equation (5):

$$k = \frac{2\pi}{\hbar} J^2 \frac{1}{\sqrt{4\pi k_B T \lambda}} e^{\frac{-(IP - EA - \Delta g_s^e - e^2/R)^2}{4 k_B T \lambda}} \quad (5)$$

where IP is the ionization potential, EA is the electron affinity, Δg_s^e is the solvation energy of the ion pair due to solvent electronic polarization, J is the electron coupling and e^2/R is ion pair Coulomb interaction energy. The reorganizational energy λ was obtained with the classical expression provided by Marcus:

$$\lambda_o = \frac{(\Delta e)^2}{2} \left(\frac{1}{a} + \frac{1}{b} - \frac{2}{R} \right) \left(\frac{1}{D_{op}} - \frac{1}{D_s} \right) \quad (6)$$

where a is the distance Bi(30)–Bi(27) = 3.32Å in the Bi_2O_3 cluster and Bi(1)–Bi(8) = 3.3Å in the $Bi_5O_7NO_3$ cluster; b is the distance C(12)–C(15) = 2.79Å in the Bi_2O_3 cluster and C(27)–C(28) = 2.79Å in the $Bi_5O_7NO_3$ cluster; R is the mean distance between Bi(30)–C(12)

and Bi(27)–C(15) in the Bi_2O_3 cluster, and it is equal to 3.62 Å; in $Bi_5O_7NO_3$, R is the mean distance between Bi(1)–C(27) and Bi(8)–C(28), and it is equal 3.51Å; $\Delta e = 2$ is the number of electrons exchanged; D_{op} and D_s are the optical and static dielectric constants of water, respectively.

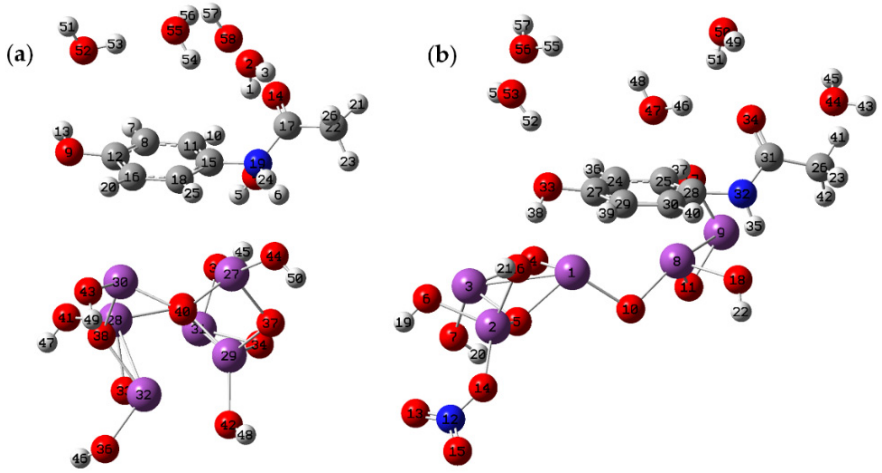

Figure 7. Optimized structures of PCM interaction with (**a**) Bi_2O_3 and (**b**) $Bi_5O_7NO_3$ representative units. Bismuth atoms are represented as purple spheres, carbon atoms as grey spheres, oxygen atoms as red spheres, nitrogen atoms as blue spheres and hydrogen atoms as white spheres.

The calculated rate constant was $k = 3.2$ ms^{-1} for $Bi_5O_7NO_3$ and $k = 1.9$ ms^{-1} for Bi_2O_3. Both theoretical values were close to the experimental ones reported in Table 4. However, the proposed computational model does not account for coupled chemical reactions such as the dimerization of NAPQI and possible diffusion limitations. For this reason, a slight overestimation of the rate constant in the theoretical model for both Bi_2O_3 and $Bi_5O_7NO_3$ is expected.

The computational studies showed a greater interaction distance between PCM and the bismuth in the case of Bi_2O_3 than that in the case of $Bi_5O_7NO_3$. The tight interaction between PCM and $Bi_5O_7NO_3$ is one possible reason for the increased electron transfer, as is also demonstrated by Table 3. On the other hand, that was also likely limited by the desorption of the oxidized PCM, as is demonstrated in cyclic voltammetry experiments by the dependence of I_{pc}/I_{pa} on the concentration of PCM. Heterostructures of $Bi_2O_3/Bi_5O_7NO_3$ seem to mitigate this issue by providing a better balance between the adsorption of reduced species and the desorption of oxidized products due to a more disordered surface topography.

4. Conclusions

In this work, we reported a systematic study on the effect of the production temperature on the electrochemical performances of bismuth subnitrate species, evaluating their electron transfer rate constant through empirical data using the Laviron model and semiempirical computational methods.

Furthermore, we have shown that it is possible to follow the progressive oxidation of a bismuth subnitrate through the Raman spectroscopy. Consequently, the intensity of the NO_3^- symmetric stretching peak at a Raman shift of 1049 cm^{-1} was observed to inversely correlate with the calcination temperature. This allowed us to monitor the transition of $Bi_5O_7NO_3$ to pure Bi_2O_3 through bismuth subnitrate heterostructures.

A comprehensive characterization of the modified SPEs compared to the bare electrode was provided through cyclic voltammetry measurements. Enhancements in (anodic–cathodic) peak currents were noticed for all the SPEs. The introduction of deliberate defects into the structure of the subnitrate, in the form of partial oxidation sites, was shown to favor an improved electron transfer. The heterostructure B500 caused the greatest improvement

to the carbonaceously working electrode in terms of its sensitivity and kinetics. We also evaluated the interaction of modified SPEs with PCM through a computational study, identifying the geometrical factors that maximized the electron transfer rate. The computational study showed that the presence of nitric residues induced geometrical constraints on the transitional state, but also that it is still more energetically favorable compared with pure bismuth oxide. This suggest that a combination of bismuth oxide and bismuth subnitrate could give rise to the synergistic effects observed.

This work lays the foundation for future developments of defective-bismuth-tailored SPEs with improved responses in non-enzymatic sensing.

Author Contributions: Conceptualization, M.B., A.T. and S.C.; methodology, F.F. and M.B.; software, F.F.; formal analysis, F.F. and M.B.; investigation, F.F., M.B., A.T. and S.C.; resources, A.T. and S.C.; data curation, F.F.; writing—original draft preparation, F.F., M.B., A.T. and S.C.; writing—review and editing, F.F., M.B., A.T. and S.C.; visualization, F.F.; supervision, A.T. and S.C. All authors have read and agreed to the published version of the manuscript.

Funding: This research received no external funding.

Data Availability Statement: Not applicable.

Conflicts of Interest: The authors declare no conflict of interest.

References

1. Chiam, E.; Weinberg, L.; Bellomo, R. Paracetamol: A review with specific focus on the haemodynamic effects of intravenous administration. *Heart Lung Vessel.* **2015**, *7*, 121.
2. Przybyła, G.W.; Szychowski, K.A.; Gmiński, J. Paracetamol—An old drug with new mechanisms of action. *Clin. Exp. Pharmacol. Physiol.* **2021**, *48*, 3–19. [CrossRef] [PubMed]
3. Graham, G.G.; Scott, K.F. Mechanism of action of paracetamol. *Am. J. Ther.* **2005**, *12*, 46–55. [CrossRef]
4. Graham, G.G.; Davies, M.J.; Day, R.O.; Mohamudally, A.; Scott, K.F. The modern pharmacology of paracetamol: Therapeutic actions, mechanism of action, metabolism, toxicity and recent pharmacological findings. *Inflammopharmacology* **2013**, *21*, 201–232. [CrossRef] [PubMed]
5. Stravitz, R.T.; Lee, W.M. Acute liver failure. *Lancet* **2019**, *394*, 869–881. [CrossRef]
6. Murray, K.E.; Thomas, S.M.; Bodour, A.A. Prioritizing research for trace pollutants and emerging contaminants in the freshwater environment. *Environ. Pollut.* **2010**, *158*, 3462–3471. [CrossRef]
7. Żur, J.; Piński, A.; Marchlewicz, A.; Hupert-Kocurek, K.; Wojcieszyńska, D.; Guzik, U. Organic micropollutants paracetamol and ibuprofen—Toxicity, biodegradation, and genetic background of their utilization by bacteria. *Environ. Sci. Pollut. Res.* **2018**, *25*, 21498–21524. [CrossRef]
8. Gogate, P.R.; Pandit, A.B. A review of imperative technologies for wastewater treatment I: Oxidation technologies at ambient conditions. *Adv. Environ. Res.* **2004**, *8*, 501–551. [CrossRef]
9. Merciai, R.; Guasch, H.; Kumar, A.; Sabater, S.; García-Berthou, E. Trace metal concentration and fish size: Variation among fish species in a Mediterranean river. *Ecotoxicol. Environ. Saf.* **2014**, *107*, 154–161. [CrossRef]
10. Elersek, T.; Milavec, S.; Korošec, M.; Brezovsek, P.; Negreira, N.; Zonja, B.; de Alda, M.L.; Barceló, D.; Heath, E.; Ščančar, J. Toxicity of the mixture of selected antineoplastic drugs against aquatic primary producers. *Environ. Sci. Pollut. Res.* **2016**, *23*, 14780–14790. [CrossRef]
11. Alanazi, K.; Cruz, A.G.; Di Masi, S.; Voorhaar, A.; Ahmad, O.S.; Cowen, T.; Piletska, E.; Langford, N.; Coats, T.J.; Sims, M.R. Disposable paracetamol sensor based on electroactive molecularly imprinted polymer nanoparticles for plasma monitoring. *Sens. Actuators B Chem.* **2021**, *329*, 129128. [CrossRef]
12. Claussen, J.; Shi, J.; Rout, C.S.; Artiles, M.; Roushar, M.; Stensberg, M.; Porterfield, D.M.; Fisher, T. Nano-sized biosensors for medical applications. In *Biosensors for Medical Applications*; Elsevier: Amsterdam, The Netherlands, 2012; pp. 65–102.
13. Maduraiveeran, G.; Jin, W. Nanomaterials based electrochemical sensor and biosensor platforms for environmental applications. *Trends Environ. Anal. Chem.* **2017**, *13*, 10–23. [CrossRef]
14. Roduner, E. Size matters: Why nanomaterials are different. *Chem. Soc. Rev.* **2006**, *35*, 583–592. [CrossRef] [PubMed]
15. Sasidharan, S.; Raj, S.; Sonawane, S.; Sonawane, S.; Pinjari, D.; Pandit, A.; Saudagar, P. Nanomaterial synthesis: Chemical and biological route and applications. In *Nanomaterials Synthesis*; Elsevier: Amsterdam, The Netherlands, 2019; pp. 27–51.
16. Kang, X.; Wang, J.; Wu, H.; Liu, J.; Aksay, I.A.; Lin, Y. A graphene-based electrochemical sensor for sensitive detection of paracetamol. *Talanta* **2010**, *81*, 754–759. [CrossRef]
17. Li, Z.-Y.; Gao, D.-Y.; Wu, Z.-Y.; Zhao, S. Simultaneous electrochemical detection of levodopa, paracetamol and l-tyrosine based on multi-walled carbon nanotubes. *RSC Adv.* **2020**, *10*, 14218–14224. [CrossRef]

18. Annadurai, K.; Sudha, V.; Murugadoss, G.; Thangamuthu, R. Electrochemical sensor based on hydrothermally prepared nickel oxide for the determination of 4-acetaminophen in paracetamol tablets and human blood serum samples. *J. Alloys Compd.* **2021**, *852*, 156911. [CrossRef]
19. Veloso, A.; Cheng, X.; Kerman, K. Electrochemical biosensors for medical applications. In *Biosensors for Medical Applications*; Elsevier: Amsterdam, The Netherlands, 2012; pp. 3–40.
20. Wu, W.; Huang, Z.-H.; Lim, T.-T. Recent development of mixed metal oxide anodes for electrochemical oxidation of organic pollutants in water. *Appl. Catal. A Gen.* **2014**, *480*, 58–78. [CrossRef]
21. Xie, C.; Yan, D.; Chen, W.; Zou, Y.; Chen, R.; Zang, S.; Wang, Y.; Yao, X.; Wang, S. Insight into the design of defect electrocatalysts: From electronic structure to adsorption energy. *Mater. Today* **2019**, *31*, 47–68. [CrossRef]
22. Bartoli, M.; Jagdale, P.; Tagliaferro, A. A Short Review on Biomedical Applications of Nanostructured Bismuth Oxide and Related Nanomaterials. *Materials* **2020**, *13*, 5234. [CrossRef]
23. Gadhi, T.A.; Hernández, S.; Castellino, M.; Jagdale, P.; Husak, T.; Hernández-Gordillo, A.; Tagliaferro, A.; Russo, N. Insights on the role of β-Bi_2O_3/$Bi_5O_7NO_3$ heterostructures synthesized by a scalable solid-state method for the sunlight-driven photocatalytic degradation of dyes. *Catal. Today* **2019**, *321–322*, 135–145. [CrossRef]
24. Kodama, H. Synthesis of a new compound, Bi5O7NO3, by thermal decomposition. *J. Solid State Chem.* **1994**, *112*, 27–30. [CrossRef]
25. Madagalam, M.; Bartoli, M.; Tagliaferro, A.; Carrara, S. Bismuth-nanocomposites modified SPCEs for non-enzymatic electrochemical sensors. *IEEE Sens. J.* **2021**, *21*, 11155–11162. [CrossRef]
26. Bard, A.J.; Faulkner, L.R. *Electrochemical Methods: Fundamentals and Applications*; Wiley: New York, NY, USA, 1980.
27. Harwig, H. On the Structure of Bismuthsesquioxide: The α, β, γ, and δ-Phase. *Z. Für Anorg. Allg. Chem.* **1978**, *444*, 151–166. [CrossRef]
28. Ziegler, P.; Ströbele, M.; Meyer, H.-J. Crystal structure of pentabismuth heptaoxide nitrate, Bi5O7NO3. *Z. Für Krist. New Cryst. Struct.* **2004**, *219*, 91–92. [CrossRef]
29. Syrovaya, A.O.; Levashova, O.L.; Andreeva, S.V. Investigation of quantum-chemical properties of paracetamol. *J. Chem. Pharm. Res.* **2015**, *7*, 307–311.
30. Marcus, R.A. Chemical and electrochemical electron-transfer theory. *Annu. Rev. Phys. Chem.* **1964**, *15*, 155–196. [CrossRef]
31. Tachiya, M. Generalization of the Marcus equation for the electron-transfer rate. *J. Phys. Chem.* **1993**, *97*, 5911–5916. [CrossRef]
32. Xu, M.; Larentzos, J.P.; Roshdy, M.; Criscenti, L.J.; Allen, H.C. Aqueous divalent metal–nitrate interactions: Hydration versus ion pairing. *Phys. Chem. Chem. Phys.* **2008**, *10*, 4793–4801. [CrossRef]
33. Madelung, O.; Rössler, U.; Schulz, M. Bismuth oxide (Bi_2O_3) IR absorption bands, Raman spectra. In *Non-Tetrahedrally Bonded Elements and Binary Compounds I*; Springer: Berlin, Germany, 1998; pp. 1–4.
34. Hardcastle, F.D.; Wachs, I.E. The molecular structure of bismuth oxide by Raman spectroscopy. *J. Solid State Chem.* **1992**, *97*, 319–331. [CrossRef]
35. Balint, R.; Bartoli, M.; Jagdale, P.; Tagliaferro, A.; Memon, A.S.; Rovere, M.; Martin, M. Defective Bismuth Oxide as Effective Adsorbent for Arsenic Removal from Water and Wastewater. *Toxics* **2021**, *9*, 158. [CrossRef]
36. Miner, D.J.; Rice, J.R.; Riggin, R.M.; Kissinger, P.T. Voltammetry of acetaminophen and its metabolites. *Anal. Chem.* **1981**, *53*, 2258–2263. [CrossRef]
37. Nematollahi, D.; Shayani-Jam, H.; Alimoradi, M.; Niroomand, S. Electrochemical oxidation of acetaminophen in aqueous solutions: Kinetic evaluation of hydrolysis, hydroxylation and dimerization processes. *Electrochim. Acta* **2009**, *54*, 7407–7415. [CrossRef]
38. Elgrishi, N.; Rountree, K.J.; McCarthy, B.D.; Rountree, E.S.; Eisenhart, T.T.; Dempsey, J.L. A practical beginner's guide to cyclic voltammetry. *J. Chem. Educ.* **2018**, *95*, 197–206. [CrossRef]
39. Mirceski, V.; Stojanov, L.; Ogorevc, B. Step potential as a diagnostic tool in square-wave voltammetry of quasi-reversible electrochemical processes. *Electrochim. Acta* **2019**, *327*, 134997. [CrossRef]
40. Laviron, E. General expression of the linear potential sweep voltammogram in the case of diffusionless electrochemical systems. *J. Electroanal. Chem. Interfacial Electrochem.* **1979**, *101*, 19–28. [CrossRef]
41. Wu, J.; Chen, T.; Zhu, C.; Du, J.; Huang, L.; Yan, J.; Cai, D.; Guan, C.; Pan, C. Rational Construction of a WS_2/CoS_2 Heterostructure Electrocatalyst for Efficient Hydrogen Evolution at All pH Values. *ACS Sustain. Chem. Eng.* **2020**, *8*, 4474–4480. [CrossRef]
42. Wu, Y.; Li, F.; Chen, W.; Xiang, Q.; Ma, Y.; Zhu, H.; Tao, P.; Song, C.; Shang, W.; Deng, T.; et al. Coupling Interface Constructions of MoS_2/$Fe_5Ni_4S_8$ Heterostructures for Efficient Electrochemical Water Splitting. *Adv. Mater.* **2018**, *30*, 1803151. [CrossRef] [PubMed]
43. Jing, Y.; Mu, X.; Xie, C.; Liu, H.; Yan, R.; Dai, H.; Liu, C.; Zhang, X.-D. Enhanced hydrogen evolution reaction of WS_2–CoS_2 heterostructure by synergistic effect. *Int. J. Hydrogen Energy* **2019**, *44*, 809–818. [CrossRef]